Physics and Chemistry of Minerals (2018) 45:831–842
https://doi.org/10.1007/s00269-018-0965-y

ORIGINAL PAPER

Single crystal growth, crystalline structure investigation and high-pressure behavior of impurity-free siderite ($FeCO_3$)

Wen Liang[1] · Yuan Yin[1,2] · Zeming Li[1,2] · Rui Li[1,2] · Lin Li[3] · Yu He[1,4] · Haini Dong[4] · Zengsheng Li[5] · Shuai Yan[6] · Shuangmeng Zhai[1] · Heping Li[1]

Received: 29 November 2017 / Accepted: 21 March 2018 / Published online: 29 March 2018

Abstract

Single crystals of impurity-free siderite were grown successfully using high-temperature–pressure annealing. The size of crystals ranged up to 100 μm, and they exhibited a rhomboid shape upon cleavage along the (101) plane. The composition of $Fe_{0.9988\pm0.0011}CO_3$ was quantified using electron probe analysis. Accurate crystalline structural data were investigated by means of single crystal X-ray diffraction (XRD) and the unit cell dimensions obtained in the rhombohedral symmetry of the $R\bar{3}c$ space group were $a=4.6861(3)$ and $c=15.362(2)$, and the final $R=0.0499$. Using in situ synchrotron XRD, the high-pressure behavior of impurity-free siderite was investigated up to 20 GPa at ambient temperature. The pressure–volume (P–V) EoS was fitted by a third-order Birch–Murnaghan equation, and the isothermal bulk modulus was $K_0=97.5(11)$ GPa for $K_0'=4$. High-pressure Raman spectroscopy was performed at up to 30 GPa at ambient temperature, and the Raman bands shifted as the increase of pressure ($\frac{dv_i}{dP}$) was determined. In combination with the high-pressure Raman results and the bulk modulus K_0, the mode Grüneisen parameters of each vibration were calculated. Meanwhile, high-temperature Raman spectroscopy was carried out at up to 300 °C and the Raman band shift ($\frac{dv_i}{dt}$) was also quantified.

Keywords Impurity-free siderite · Single crystal growth · Single crystal X-ray diffraction · In situ synchrotron X-ray diffraction · Raman spectroscopy · High pressure

Introduction

Iron, the core component of most mantle minerals, has been widely studied in the field of geoscience. The key role of iron in the physical and chemical properties of mantle minerals is thought to arise from the various valence states and spin states exhibited by the 3d electrons under high-temperature–pressure conditions, which subsequently could give iron unique and attractive properties (McCammon 2005; Speziale et al. 2005; Sturhahn et al. 2005; Lin and Tsuchiya 2008). Recently, increased interest in the role of carbonate minerals in the global carbon cycle has resulted in a greater understanding of the high-temperature–pressure behavior of ferromagnesite ($Mg_{1-x}Fe_xCO_3$) which has become important in better understanding deep-carbon storage in the Earth's interior (Jana and Walker 1997; Dasgupta and Hirschmann 2010; Rohrbach and Schmidt 2011; Hazen et al. 2012). The large amount of research over the last few decades into the high-temperature–pressure properties of ferromagnesite has used various experimental and theoretical techniques, including in situ synchrotron XRD, Raman spectroscopy,

Electronic supplementary material The online version of this article (https://doi.org/10.1007/s00269-018-0965-y) contains supplementary material, which is available to authorized users.

✉ Heping Li
liheping@vip.gyig.ac.cn

[1] Key Laboratory of High temperature and High pressure Study of the Earth's Interior, Institute of Geochemistry, Chinese Academy of Sciences, Guiyang 550081, China

[2] University of Chinese Academy of Sciences, Beijing 100049, China

[3] China University of Geosciences, Beijing 100083, China

[4] Center for High Pressure Science and Technology Advanced Research, Shanghai 201203, China

[5] Shandong Geological Sciences Institute, Jinan 250013, China

[6] Shanghai Synchrotron Radiation Facility, Shanghai Institute of Applied Physics, Chinese Academy of Sciences, Shanghai 201800, China

and first-principles calculations (Mattila et al. 2007; Shi et al. 2008; Lavina et al. 2009, 2010a, b; Nagai et al. 2010; Farfan et al. 2012; Lin et al. 2012; Liu et al. 2014; Spivak et al. 2014; Cerantola et al. 2015, 2017; Lobanov et al. 2015; Merlini et al. 2016; Weis et al. 2017). Interestingly, the results from these studies revealed that ferromagnesite is more stable when in a dense phase under high-temperature–pressure conditions by phase transition, which would be more conducive to study the high-temperature–pressure state of the deep-carbon host in the lower mantle.

It is well supported by research that magnesite and siderite can form a complete solid solution ferromagnesite with a rhombohedral structure (Rosenberg 1963). In this regard, understanding of the end member phase is the basis of research into the whole ferromagnesite system. There has been significant research to elucidate the high-temperature–pressure properties of magnesite, including EoS, high-pressure Raman spectroscopy and Brillouin light scattering (Markgraf and Reeder 1985; Ross 1997; Williams et al. 1992; Zhang et al. 1997; Isshiki et al. 2004; Lin et al. 2012; Liu et al. 2014, 2015; Yang et al. 2014; Fu et al. 2017; Liang et al. 2018a). Impurity-free siderite is of equal research value to impurity-free magnesite due to the significance of iron element in geoscience. Impurity-free siderite gives a limiting case of the iron content (100%) in iron-rich ferromagnesite, which provides an ideal model to study the properties arising from the phase transition of iron-bearing carbonates. Although interesting experimental results about siderite have been reported recently (Cerantola et al. 2015, 2017; Weis et al. 2017), other properties deserve further investigation, including the crystalline structure, anisotropic elasticity, and anisotropic conductivity. Considering natural siderite samples always contain impurities rendering them unsuitable for the quantitative requirements of the end member phase studies, artificial growth of large single siderite crystals with high purity is absolutely essential to adequately study siderite.

The single crystal growth of impurity-free siderite is a difficult proposition and, to date, has only been successfully reported by Cerantola et al. (2015), with single crystals reaching up to 50 μm in maximal size. However, to determine accurate crystal orientation, the production of much larger high-purity single crystals is essential for the quantitative study of anisotropic properties, including elastic C_{ij} and conductivity σ_{ij}. Moreover, standard structural mineralogical data of siderite have to be achieved from XRD results of high-purity and high-quality single crystals. Hence, the artificial growth of single siderite crystals remains worthy of further improvement due to the research significance of iron-bearing carbonates.

This paper reports a general and reproducible method to improve artificial single crystal growth of impurity-free siderite. Using high-temperature–pressure annealing, high-quality single crystals of impurity-free siderite were achieved, and significantly, the size of the single crystals reached 100 μm. The structural data and composition of the single crystals we obtained were determined using single crystal XRD and electron probe analysis. Its high-pressure properties were investigated by Raman spectroscopy and in situ synchrotron XRD.

Experimental method

Single crystal siderite was grown by high-temperature–pressure annealing in a sealed environment. The process consisted of two parts: nucleation and growth.

For single crystal nucleation, Fe_2O_3 (99.99%, Alfa Aesar) and anhydrous $H_2C_2O_4$ (98%, Alfa Aesar) were mixed (molar ratio 1:2) and then ground in an agate mortar. The sample pellet was prepared and sealed in a platinum capsule (6 mm diameter, 3 mm length, 0.1 mm thickness) with deionized water (30 μL). Using h-BN as pressure medium, the high-pressure synthesis was performed on a DS 6 × 600 t cubic-anvil-type apparatus at 3 GPa and 800 °C for 12 h, after which the reaction was quenched to room temperature and the pressure released. The platinum capsule was opened and the small single crystals (5–10 μm) were examined under a microscope.

For single crystal growth, small single crystals and the starting materials from the single crystal nucleation were combined (1:3 molar ratio of $FeCO_3$:Fe_2O_3), and the sample mixed, ground and sealed in a platinum capsule with more deionized water (60), as for the single crystal nucleation experiment. The sample was re-treated under microliter 1 GPa and 550 °C for 24 h, then quenched to room temperature and the pressure released. The platinum capsule was opened and the sample was removed, cleaned in alcohol by ultrasonication and air-dried. The single crystals were observed under a plane-polarized microscope, shown in Fig. 1.

Observation under the microscope showed that the size of the single crystals reached up to 100 μm, and they were bright, light yellow and had a rhombohedral habit with perfect (101) cleavage. The micro-composition of the single crystals was quantified by electron probe analysis as $Fe_{0.9988\pm0.0011}CO_3$.

Single crystal XRD measurements were conducted at ambient pressure using a four-circle Bruker diffractometer equipped with a SMART APEX-CDD detector using MoKα radiation at the China University of Geosciences, Beijing. One single crystal (~ 100 μm) was selected for the single crystal XRD experiment, with 722 reflections collected, and the reflection intensities were measured by scanning the narrow frames. The structures were solved by the direct comparison method and refined by full matrix least-squares

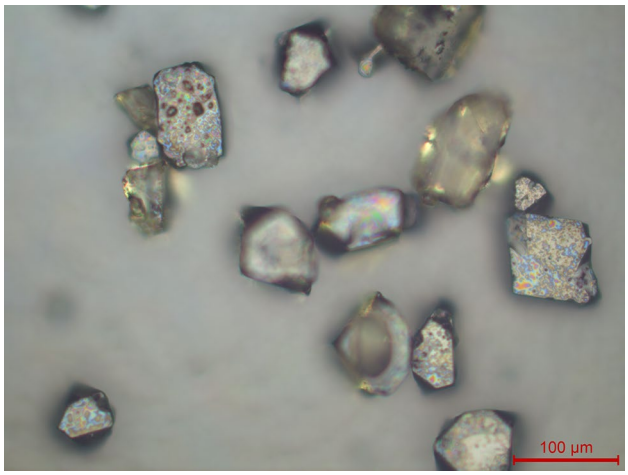

Fig. 1 The micrograph of siderite single crystals obtained at 1 GPa and 550 °C for 24 h

using SHELXTL5.1 software. The anisotropic thermal parameters were refined using the x-coordinate of oxygen.

For high-pressure in situ synchrotron XRD experiments, single crystals of siderite were ground into powder and then the powder sample was compressed into a thin slice by a diamond anvil cell (DAC). For a starting sample, a thin slice of the powder sample was cut with a diameter of ~ 100 µm and a thickness of ~ 30 µm. A rhenium gasket was indented to a thickness of 50 µm by a pair of diamond anvils with 500-µm flat culets, and then a 250-µm-diameter hole was drilled into the pre-indented gasket for use as a sample chamber. The starting sample was loaded into the sample chamber of a DAC together with several ruby spheres close to the sample as pressure calibrants. Neon was loaded into the sample chamber as the pressure medium using a high-pressure gas loader at the Center for High Pressure Science and Technology Advanced Research, Shanghai. High-pressure angle-dispersive in situ XRD was conducted using beamline BL15U-1 at the Shanghai Synchrotron Radiation Facility (Zhang et al. 2015). A monochromatic X-ray with a wavelength of 0.6199 Å was adopted, and the beam spot on the sample was 3 × 4 µm. Detectors of the beamline included a mini-ionization chamber (2 cm thickness) from ADC, USA; three ionization chambers with the electrode lengths of 5, 14 and 28 cm, from OKEN, Japan; a seven-element Si(Li) detector (e2v, USA) with high-speed XIA DXP electronics, for fluorescence detection; two single-Vortex-90EX Si drift detectors (SDD) from SII, USA, which provided excellent energy resolution and a high output counting rate (< 136eV@5:9 keV, at 100 kcps counting rate); and a Mar165 CCD, for X-ray diffraction experiments. Two-dimensional images were collected for 180 s at different pressures and integrated by Dioptas software (Prescher and Prakapenka 2015) to obtain the one-dimensional diffraction patterns. XRD data were analyzed by the GSAS program to obtain the lattice parameters (Larson and Von Dreele 2004).

For high-pressure Raman spectroscopy experiments, a piece of the single crystal with a diameter of ~ 100 µm and a thickness of ~ 30 µm was cleaved along the (101) rhombohedral plane and used as the starting sample. A rhenium gasket was indented to a thickness of 50 µm by a pair of diamond anvils with 400-µm flat culets. A 220-µm-diameter hole was drilled into the pre-indented gasket and used as a sample chamber. The starting sample was loaded into the sample chamber of a DAC with the (101) crystal plane facing the culet, together with several ruby spheres close to the sample as pressure calibrants, and neon was loaded into the sample chamber as the pressure medium.

High-temperature Raman spectroscopy data were collected on a THMSG 600 freezing/heating stage with a precision of ± 0.1 °C. The heating process was performed from ambient temperature to 300 °C (below the siderite decomposition temperature) at 20 °C increments in an argon atmosphere. Every temperature increment was maintained for 10 min to ensure temperature uniformity, and Raman spectroscopy patterns were recorded.

A Renishaw 2000 micro-confocal laser Raman spectrometer equipped with a charge-coupled device detector, a 2400 lines/mm diffraction grating, and a holographic notch filter was used. A Spectra-Physics model 2017 argon ion laser operating at 514.5 nm was used as the excitation source. The laser power was limited to 30 mW to avoid overheating of the sample and the zero-offset was calibrated using a silicon single crystal at 520.0 cm^{-1}. Scattered radiation was collected by an Olympus microscope 20× ultralong working distance objective through backscattering. Each Raman spectrum was collected for an exposure time of 10 min to ensure quality data analyses. The pressure and error thereof were quantified from the average pressure values given by the ruby spheres before and after recording each Raman spectrum.

Results and discussion

Impurity-free $FeCO_3$ single crystal growth by high-temperature–pressure annealing

Single crystal growth of $FeCO_3$ is almost impossible at ambient conditions due to its relatively poor thermal and chemical stability. However, the process of $FeCO_3$ single crystal growth is relatively easy to control under high-temperature–pressure conditions because, high-pressure not only significantly increases its thermal stability, but using a $CO + CO_2$ atmosphere also provides the necessary reducing environment in a closed cavity to promote Fe^{2+}. As early as the 1970s, the stability of siderite in a Fe–C–O system

was investigated under low pressure (500–2000 bars) in a $CO + CO_2$ atmosphere (French 1971). The results showed that siderite could be synthesized by decomposition of ferrous oxalate dihydrate ($FeC_2O_4{\cdot}2H_2O$) at 2000 bars and approximately 380 °C. Subsequently, the *P*–*T* phase diagrams arising from decomposition of $FeC_2O_4{\cdot}2H_2O$ and the thermal stability of $FeCO_3$ were systematically studied at 1–3 GPa (Liang et al. 2018b), indicating that high pressure can greatly improve the thermal stability of $FeCO_3$ and effectively increase the temperature range for decomposition of $FeC_2O_4{\cdot}2H_2O$ and formation of $FeCO_3$. Thus far, high-temperature–pressure decomposition from $FeC_2O_4{\cdot}2H_2O$ is the most direct and feasible method for the synthesis of siderite (Cerantola et al. 2015, 2017).

However, previous studies identified an essential problem of the small grain size of siderite synthesized by the high-temperature–pressure decomposition method, even following recrystallization (Cerantola et al. 2015, 2017; Liang et al. 2018b). Therefore, it was necessary to improve the process of single crystal growth.

In the field of material science, high-temperature–pressure annealing is a mature technology that has been widely used for functional material synthesis (Liu et al. 2006; Liang et al. 2013; Xia et al. 2015). The core principle of this method is to achieve doping elements with abnormal valence (for example, $Cu^{2+\delta}$, $Fe^{3+\delta}$) via redox reaction in a closed cavity under a controlled gas atmosphere and high-temperature–pressure conditions. For example, the $Sr_2CuO_{4-\sigma}$ superconductor uses O_2 atmosphere to anneal the Sr_2CO_3 precursor such that it undergoes structural transition to $Sr_2CuO_{4-\sigma}$ from the orthorhombic non-superconductivity phase to the tetragonal superconductivity phase, as well as achieving oxygen vacancy doping in the copper oxide (CuO_2) plane.

Therefore, high-temperature–pressure annealing is considered as a remarkably effective and easily repeatable way to improve the process of single crystal growth of impurity-free siderite. Based on the high-temperature–pressure decomposition of $FeC_2O_4{\cdot}2H_2O$ (see Eq. 1), $FeCO_3$ could be stable in the $CO + CO_2$ atmosphere. Accordingly, a redox reaction using the high-temperature–pressure annealing process in a closed cavity was designed as shown in Eq. 2:

$$FeC_2O_4 \cdot 2H_2O \rightarrow FeCO_3 + CO\,(g) + 2H_2O\,(g) \quad (1)$$

$$Fe_2O_3 + 2H_2C_2O_4 \rightarrow 2FeCO_3 + CO_2\,(g) + CO\,(g) + 2H_2O\,(g) \quad (2)$$

The $CO + CO_2$ annealing atmosphere is provided by the decomposition of excess $H_2C_2O_4$, whereas $FeCO_3$ is achieved from Fe_2O_3 reduction by CO under *P*–*T* conditions at which $FeCO_3$ is thermally stable (Liang et al. 2018b). Moreover, the presence of water provides the necessary $CO_2 + H_2O$ environment for single crystal growth and also greatly reduces residual stress in single crystals.

To accelerate the single crystal nucleation reaction, relatively high-temperature–pressure conditions were initially used. Nucleation at 3 GPa and 800 °C for 12 h yielded some small ~ 2–10-μm single crystals with rhomboid shape, shown in Supplementary Fig. 1(a). Subsequently, to accelerate the single crystal growth rate and to reduce the effect of high-pressure residual stress, these small crystals were re-treated by the same annealing reaction but at relatively lower temperature–pressure conditions and in the presence of more liquid H_2O. Figure 1 shows that the single crystal size reached up to 100 μm at 1 GPa and 550 °C for 24 h. As a comparative experiment, single crystal growth was carried out directly using the same starting materials (see Eq. 2) at 3 GPa and 800 °C for 36 h, producing crystals of up to ~ 50 μm, as shown in Supplementary Fig. 1(b). This indicates that higher temperature–pressure conditions are propitious to the crystal nucleation reaction, but not to single crystal growth.

The reduction environment provided by excess $H_2C_2O_4$ is equivalent to that produced through FeC_2O_4 decomposition. Based on the results of Mössbauer spectroscopy reported by Cerantola et al. (2015), any trace of Fe^{3+} was not observed in siderite single crystals synthesized from FeC_2O_4 decomposition and, therefore, the siderite crystals we obtained are not expected to contain Fe^{3+}. Besides, it would also be feasible to prepare single crystals of isotopic siderite $^{57}FeCO_3$ from the starting material $^{57}Fe_2O_3$ through high-temperature–pressure annealing, thereby solving the difficulty of ^{57}Fe isotopic sample synthesis.

Composition and morphology of the siderite single crystal

Thin sections were prepared from the siderite single crystals. Unfortunately, $FeCO_3$ single crystals are highly brittle and easily cleave during polishing so that it is not possible to achieve thin section that is perfectly smooth. Nevertheless, the thin section is used for micro-composition quantification by electron probe analysis. The backscattering electronic (BSE) image, the detection position on the thin section, and the results of Fe content analysis are given in Supplementary Fig. 2 and Table 1. When compared with BSE images using Fe_3O_4 as the standard sample, it was observed that the grayscales of the polished single crystal surfaces were almost identical, implying that the single crystals had the same Fe content. It is also worth noting that the abnormal and white parts (marked by green circles) were identified as Cr_2O_3, derived from the remnants of grinding papers. A total of 25 points in five different areas (marked by red circles) were selected for electron probe analysis. The average mass fraction of FeO obtained was $61.95 \pm 0.07\%$ and the single crystal composition was calculated as $Fe_{0.9988\pm0.0011}CO_3$,

which is within the error range for agreement with the stoichiometry.

The micrographs from the plane-polarized microscope were shown in Fig. 1 and Supplementary Fig. 1(c). The single crystal was bright, light yellow and rhombohedral in structure with a 120° edge angle and cleavage along the (101) plane, a typical cleaving behavior of natural calcite-type minerals.

Single crystal XRD and the crystal structure data of impurity-free siderite

Although single crystals of siderite have been successfully synthesized in the previous studies (Cerantola et al. 2015), the crystal structure data of impurity-free siderite, which is a standard database for the study of siderite, have not been determined. Using a piece of siderite crystal (~ 100 μm), single crystal XRD was carried out, enabling determination of the crystalline structural data of impurity-free siderite. The intensities of a number of reflections without splitting or trailing were collected from single crystal XRD to ensure accuracy, shown in Supplementary Fig. 3. Crystal data and structural refinement, including lattice parameters, positional and thermal parameters, and bond length and angle, are summarized in Table 1, together with crystal data of the impurity-free magnesite for comparison (Liang et al. 2018a). The crystal structure of siderite has been formatted into a CIF file, which is attached as supplementary material. Figure 2a shows the rhombohedral crystal structure of siderite as well as the coordination relations. The rhombohedral siderite unit cell consists of CO_3^{2-} anions and Fe^{2+} cations; the central Fe^{2+} cation is six coordinated with a distorted (FeO_6) octahedral geometry.

From the crystal structural data, it can be observed that the lattice parameters, cell volume and theoretical density of siderite are much larger than for magnesite. Comparison between the O–Fe–O bond angle 87.92(5)° and the O–Mg–O bond angle 88.179(11)° indicated that the (FeO_6) octahedral geometry is more twisted than the (MgO_6) octahedral geometry. Additionally, the larger ionic radius of siderite makes the Fe–O bond length 2.141(2) Å, which is considerably longer than the Mg–O bond length of 2.0976(4) Å. In contrast, the C–O bond length changes very little from 1.2846(7) Å to 1.287(4) Å, which also implies that the C–O bond is very strong and that the CO_3^{2-} anion is difficult to compress or stretch by cationic substitution in carbonate minerals.

The structural data of all previously reported $FeCO_3$–$MgCO_3$ carbonate systems, including natural and synthetic samples, are summarized in Supplementary Table 2. It can be observed that the lattice parameters of single crystals are smaller than that of synthetic polycrystals, but single crystal data, which include more structural information, are likely to be more reliable and credible than the results from polycrystal samples. It is known that siderite and magnesite can form a complete solid solution $Mg_{1-x}Fe_xCO_3$ with a rhombohedral structure. Therefore, it was assumed that the ideal solution model could be applied, and that the lattice parameters should be linearly dependent on iron solid solubility. In $Mg_{1-x}Fe_xCO_3$ complete solid solution, the ideal linear relationship between the lattice parameters and iron solid solubility x could be determined by two end members, impurity-free magnesite and siderite, which were fitted as follows, shown in Fig. 2b along with the results of previous studies.

$$a(x) = 4.6255 + 6.06 \times 10^{-2}x$$

$$c(x) = 14.987 + 3.75 \times 10^{-1}x$$

$$V(x) = 277.69 + 14.46x$$

It can be seen from Fig. 2b that all unit cell volumes of the natural samples were slightly larger than shown by the ideal solid solution calculations as the function of iron solid solubility x. One possible reason is that Shannon effective ionic radii of Mn^{2+} and Ca^{2+} were much larger than Mg^{2+} (Shannon and Prewitt 1969), so that all unit cell volumes of natural samples, which always contained minor impurities of Mn^{2+} or Ca^{2+}, were larger than those calculated from an ideal linear relationship fitted by impurity-free end members. Another potential explanation is that, in spite of the fact that $Mg_{1-x}Fe_xCO_3$ system is thought to be a complete solid solution, indeed, no single crystal structural data to date have proven that an ideal solution model applies. The system may deviate from an ideal linear relationship due to the mismatch of local lattice, distribution of misfit dislocation or ordering/disordering effect by the substitution of Mg^{2+} and Fe^{2+}. It is proposed that preparation of a series of pure $Mg_{1-x}Fe_xCO_3$ single crystals with various iron content x would enable systematic study of the $Mg_{1-x}Fe_xCO_3$ system to make clear whether these were consistent with the ideal solution model.

P–V EoS of impurity-free siderite

The elastic properties of minerals, which depend on chemical composition, crystal structure, pressure and temperature, are an important aspect of mineralogy. Among studies establishing the compositional effect of iron content on elastic properties, ferromagnesite $Mg_{1-x}Fe_xCO_3$ solid solution has been investigated extensively because of its importance in understanding carbon storage in the Earth's interior. The impurity-free siderite, as a limiting case of the iron content (100%), would provide an ideal model by which to study the elastic properties resulting entirely from the properties of iron in carbonate minerals.

Table 1 $FeCO_3$ single crystal structure

Space group $R\bar{3}c$ (no. 167)						
Lattice parameters						
$FeCO_3$ (this work)						
a	*c*	*α*	*β*	*γ*	*V*	*R*
4.6861(3)	15.362(2)	90	90	120	292.15(5)	0.0499
$MgCO_3$ (Liang et al. 2018a)						
a	*c*	*α*	*β*	*γ*	*V*	*R*
4.6255(3)	14.987(2)	90	90	120	277.69(4)	0.0243

Positional and thermal parameters of $FeCO_3$			
Parameters	Fe	C	O
x	0	0	0.2757(8)
y	0	0	0
z	0	0.25	0.25
U11	0.0021(5)	0.004(2)	0.0017(11)
U22	0.0021(5)	0.004(2)	0.0047(16)
U33	0.0025(7)	0.003(3)	0.0064(15)
U23	0.0000	0.0000	−0.0014(12)
U13	0.0000	0.0000	−0.0007(6)
U12	0.0010(3)	0.0021(12)	0.0024(8)

Bond length (Å) and bond angle (°) $FeCO_3$ (this work)	
Fe–O	2.141(2)
C–O	1.287(4)
O1–Fe–O2	87.92(5)
O1–Fe–O6	92.08(5)
O1–Fe–O5	180.000(1)
$MgCO_3$ (Liang et al. 2018a)	
Mg–O	2.0976(4)
C–O	1.2846(7)
O1–Mg–O2	88.179(11)
O1–Mg–O6	91.821(11)
O1–Mg–O5	180.000(13)

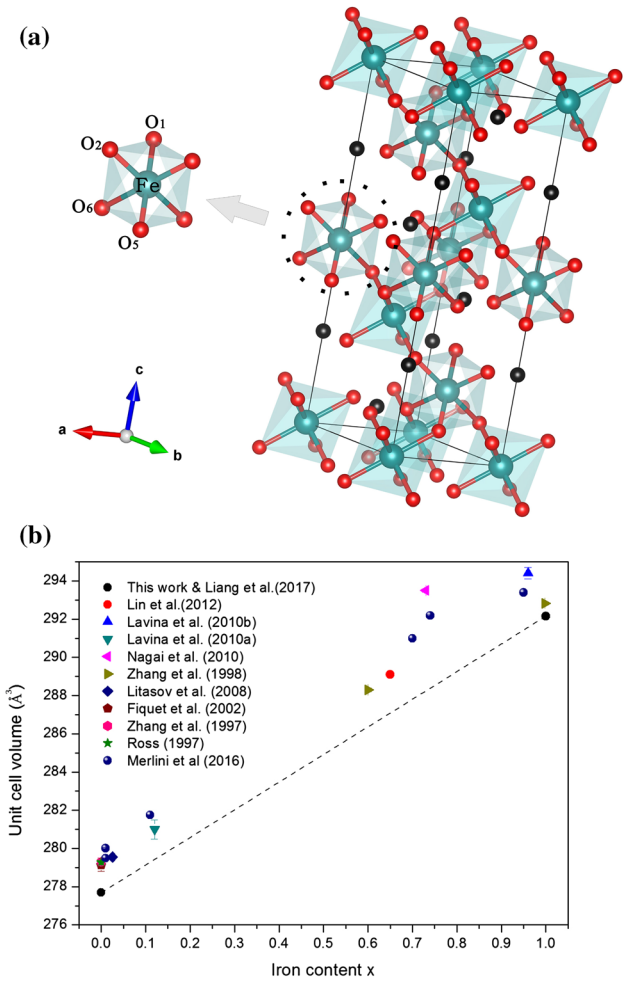

Fig. 2 **a** The rhombohedral structure of siderite crystal as well as the coordination relations. **b** The ideal linear relationship between the unit cell volume and iron solid solubility x, along with the previous studies in natural ferromagnesite

The relationship between the unit cell parameters of impurity-free siderite and pressure is shown in Fig. 3a, b together with the previous results, and the data are included in Supplementary Table 3(a). The unit cell parameters show a consistent decrease with increasing pressure in the experimental pressure range. Here the coefficient of compressibility β can be defined as $\beta = 1/V_0\, \mathrm{d}V/\mathrm{d}P$, where V_0 is the molar volume at 0 GPa. To determine its coefficient of compressibility, the P–V state equation at ambient temperature can be fitted with the quadratic function as follows:

$$a(P) = 4.6966\,[1 + (-2.025 \times 10^{-3} + 1.462 \times 10^{-5}P) \times P],$$
$$\beta a = -2.025 \times 10^{-3} + 1.462 \times 10^{-5}P,$$

$$c(P) = 15.3867\,[1 + (-5.069 \times 10^{-3} + 5.513 \times 10^{-5}P) \times P],$$
$$\beta c = -5.069 \times 10^{-3} + 5.513 \times 10^{-5}P,$$

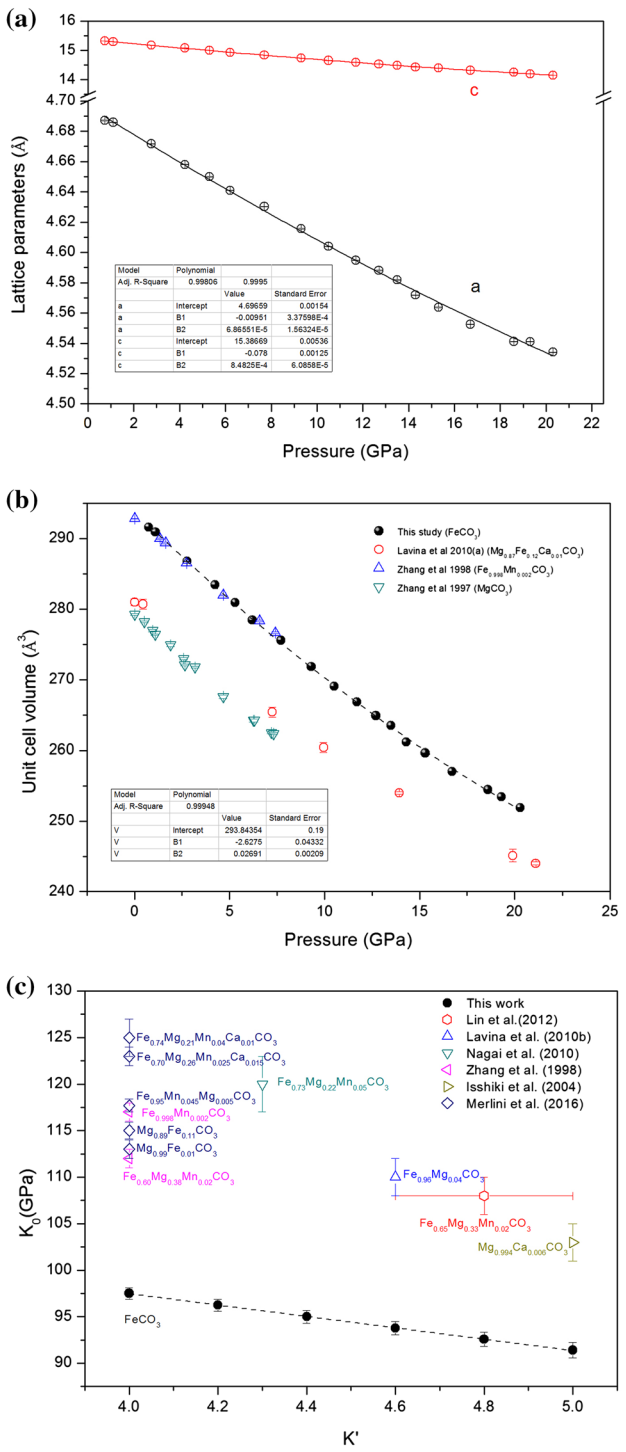

Fig. 3 **a** The relationship between the unit cell parameters (a and c) of impurity-free siderite and pressure. **b** The relationship between the unit cell volume of impurity-free siderite and pressure, together with the previous studies. **c** The various K_0 values fitted by different values of K_0' from 4 to 5, together with the previous studies

$V(P) = 293.84\ [1 + (-8.941 \times 10^{-3} + 9.158 \times 10^{-5} P) \times P]$,

$\beta_V = -8.941 \times 10^{-3} + 9.158 \times 10^{-5} P$.

The calculation of axial-pressure compressibility identifies an obvious anisotropy, and the approximative relation $\beta_V \approx 2\beta a + \beta c$ for the rhombohedral structure is observed. Calculated from $\beta c/\beta a$, the coefficient of compressibility along the c-axis is ~2.5 times greater than along the a-axis, which is consistent with the previous results of ferromagnesite (Lavina et al. 2010b). This is in reasonable agreement with the relationship between the thermal expansion coefficients, that along the c-axis ($\alpha_c = 7.995 \times 10^{-6}$/°C) being ~2.5 times more than that the along the a-axis ($\alpha_a = 3.313 \times 10^{-6}$/°C), as found by previous studies (Liang et al. 2018b):

$$a(t) = 4.695\ (1 + 3.313 \times 10^{-6} t), \quad \alpha_a = 3.313 \times 10^{-6}/°\mathrm{C},$$

$$c(t) = 15.396\ (1 + 7.995 \times 10^{-6} t), \quad \alpha_c = 7.995 \times 10^{-6}/°\mathrm{C},$$

$$V(t) = 293.92\ (1 + 1.47 \times 10^{-5} t), \quad \alpha_V = 1.47 \times 10^{-5}/°\mathrm{C}.$$

These results indicate that pure siderite has obvious anisotropy but similar anisotropic ratios of pressure compressibility and thermal expansion, which could completely depend on the elastic and thermal properties of Fe–O and C–O bonds. This conclusion would be further verified by future studies with more accurate single crystal structural data from high-temperature and high-pressure in situ single crystal XRD.

To fit isothermal compression data, a third-order Birch–Murnaghan equation of state was used to derive the bulk modulus at ambient temperature (K_0) and its pressure derivative (K_0'), which is given by:

$$P = \frac{3K_0}{2}\left[\left(\frac{V_0}{V}\right)^{\frac{7}{3}} - \left(\frac{V_0}{V}\right)^{\frac{5}{3}}\right]\left\{\left[1 - \frac{3}{4}(4 - K_0')\left[\left(\frac{V_0}{V}\right)^{\frac{2}{3}} - 1\right]\right]\right\}$$

where P is pressure, V is the unit cell volume, and the bulk modulus K_0 is calculated from the derived K_0'. The bulk modulus K_0 is calculated as 97.5(11) GPa when K_0' is 4, and the various K_0 values fitted using different values of K_0' from 4 to 5 are listed in Supplementary Table 3(b) (K_0 values are known to be closely dependent on the values of K_0').

To facilitate comparison, the linear relationship between K_0 as a function of K_0' is shown in Fig. 3c, along with results from previous studies. The K_0 values of impurity-free siderite obtained for the different K_0' values are the smallest reported for the $Mg_{1-x}Fe_xCO_3$ system to date. This indicates that impurity-free siderite has the greatest compressibility due to having the longest Fe–O and C–O bond lengths, which is consistent with knowledge that longer bonds are easier to compress. In contrast, the crystal structural data of another end phase, impurity-free magnesite, which has shorter Mg–O and C–O bond lengths than the corresponding bonds of impurity-free siderite, show that it is the most difficult to compress in the $Mg_{1-x}Fe_xCO_3$ system. Combining our findings together with the results reported for impurity-free magnesite (Markgraf and Reeder 1985; Zhang et al. 1997; Litasov et al. 2008) indicates that impurity-free siderite has the largest compressibility coefficient but the smallest thermal expansion coefficient in the ferromagnesite system, which is consistent with previously suggested compression mechanisms (Hazen and Prewitt 1977; Hazen and Finger 1982).

An important issue is that this conclusion is contrary to the results of Zhang et al. (1998), despite the very similar compositions of siderite used in both studies. Zhang et al. observed that the K_0 of siderite (117 GPa) is much larger than that of magnesite (103 GPa), which means that siderite has a longer Fe–O bond length than magnesite but is less compressible, and that this result was inconsistent with the general compression mechanisms (Hazen and Prewitt 1977; Hazen and Finger 1982). However, if this conclusion is correct, it leads to a surprising inference: the longer bond length (Fe–O) is difficult to compress and to thermally expand, while the shorter bond length (Mg–O) is easy to compress and to thermally expand. If this were the case, magnesite would be very unstable at high-temperature–pressure conditions, which is not consistent with general knowledge. In fact, as seen from Fig. 3b, the P–V data reported from Zhang et al. (1998) are very close to our results and, therefore, the big difference in K_0 value could be caused by fitting error due to the measuring range of pressure being not enough.

Furthermore, by comparison of results from previous EoS studies on the $Mg_{1-x}Fe_xCO_3$ system, it is difficult to find a systematic and unified rule for the properties of elasticity $K_0(x)$ associated with the various iron content x. The K_0 of siderite (97.5 GPa) is the lowest for iron-bearing carbonates reported so far, which implies that the increase in iron content could increase the compressibility of ferromagnesite due to a longer (Fe/Mg)–O bond length. Significantly, the density of iron-rich ferromagnesite increases dramatically with an increase of pressure, and iron-rich ferromagnesite could stabilize as a rather more dense phase in Earth's deep interior, which could cause high-conductivity and low-velocity zone. Based on this, it is proposed that a systematic study involving synthesis of a series of $Mg_{1-x}Fe_xCO_3$ single crystal samples will allow the determination of accurate structural data and elasticity properties $K_0(x)$ as it is clear that natural samples cannot provide the reliable and credible results needed to establish an elastic model in $Mg_{1-x}Fe_xCO_3$ system.

High-pressure Raman spectroscopy and the mode Grüneisen parameters

Raman spectra are already well known for calcite-type minerals (Rutt and Nicola 1974; Edwards et al. 2005; Gunasekaran et al. 2006; Rividi et al. 2010; Kaabar et al. 2011). The Raman spectrum of the siderite single crystal was measured at ambient conditions. There were five Raman active vibrations (*T, L,* ν_4, ν_1, $2\nu_2$) in the wavelength range of 100–2000 cm^{-1} at 181, 282, 738, 1084, and 1722 cm^{-1}, as shown in Fig. 4a; these were fitted with a Lorentzian function. The peaks at 181 and 282 cm^{-1} were derived mainly from translational lattice mode T and librational lattice mode L, respectively. The peaks at 738, 1084 and 1762 cm^{-1} were attributable to the in-plane bending internal mode ν_4, the symmetric stretching internal mode ν_1, and out-of-plane bending mode $2\nu_2$, respectively. The anti-symmetric stretching mode ν_3, probably located around 1445 cm^{-1}, was too weak to be observed.

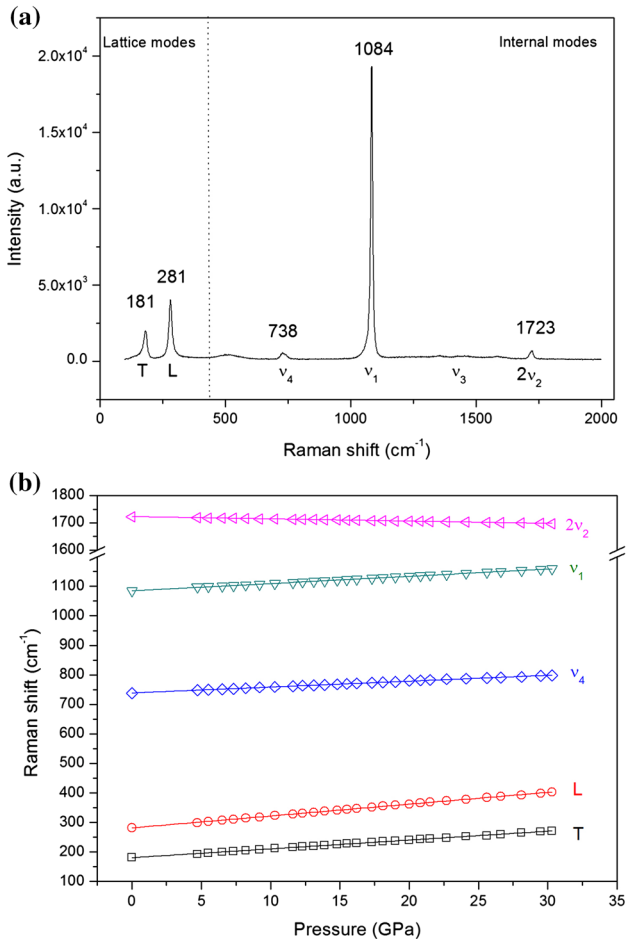

Fig. 4 **a** Raman spectra of siderite single crystals at ambient conditions. **b** High-pressure Raman spectra of siderite at ambient temperature

Subsequently, the high-pressure Raman spectrum of the siderite single crystal was measured at up to 30 GPa with pressure increased in ~ 1 GPa increments at ambient temperature. In this pressure range, four Raman active bands (*T, L,* ν_4, and ν_1) increased monotonically and almost linearly with increasing pressure and did not undergo any resolvable splitting. In contrast, $2\nu_2$ decreased linearly with increasing pressure. The linear relationship between each measured vibrational frequency ν_i and pressure P, given in Fig. 4b and data shown in Supplementary Table 4, can be fitted as follows:

$$T(P) = 180.61\ (1 + 1.656 \times 10^{-2}P), \quad V_{T,P} = 1.656 \times 10^{-2},$$

$$L(P) = 281.91\ (1 + 1.422 \times 10^{-2}P), \quad V_{L,P} = 1.422 \times 10^{-2},$$

$$\nu_4(P) = 738.48\ (1 + 2.740 \times 10^{-3}P), \quad V\nu_{4,P} = 2.740 \times 10^{-3},$$

$$\nu_1(P) = 1084.49\ (1 + 2.269 \times 10^{-3}P), \quad V\nu_{1,P} = 2.269 \times 10^{-3},$$

$$2\nu_2(P) = 1722.57\ (1 - 4.784 \times 10^{-4}P), \quad V_2\nu_{2,P} = -4.784 \times 10^{-4}.$$

Calcite-type carbonate minerals ACO_3 (A = Ca, Mg, Fe, Mn) have a common rhombohedral structure with a common feature of the carbonate ions CO_3^{2-} bound to the crystal lattice by strong internal C–O bonds and weaker A–O bonds, shown in Fig. 2a. From previous studies, it is known that all Raman active vibrations (*T, L,* ν_4, ν_1, ν_3, $2\nu_2$) depend on the carbonate ion configuration and (AO_6) octahedral geometry (Bischoff et al. 1985; Schauble et al. 2006). Therefore, Raman frequency ν_i is very closely correlated with C–O and A–O bond length. For this reason, here the rate of shift for each Raman frequency is defined as $V_{\nu i,P} = 1/\nu_{i,0}\ (d\nu_i/dP)$, which could be used as an indirect estimate of the A–O and C–O bond length compression ratio. Comparison with the results from high-pressure Raman spectra of impurity-free magnesite single crystal (Liang et al. 2018a), fitted as:

$$T(P) = 214.76\ (1 + 1.432 \times 10^{-2}P), \quad V_{T,P} = 1.432 \times 10^{-2},$$

$$L(P) = 331.65\ (1 + 1.355 \times 10^{-2}P), \quad V_{L,P} = 1.355 \times 10^{-2},$$

$$\nu_4(P) = 736.57\ (1 + 2.486 \times 10^{-3}P), \quad V\nu_{4,P} = 2.486 \times 10^{-3},$$

$$\nu_1(P) = 1094.04\ (1 + 1.674 \times 10^{-3}P), \quad V\nu_{1,P} = 1.674 \times 10^{-3},$$

shows that all $V\nu_{i,P}$ for siderite (*T, L,* ν_4, and ν_1) are much larger than the corresponding $V\nu_{i,P}$ for magnesite. From this, it can be deduced that the compression ratio of Fe–O is larger than that of Mg–O, which is also in agreement with the EoS results described above.

In addition, an anomalous result is observed: out-of-plane bending $2\nu_2$ decreased linearly with increasing pressure, which is different from the pressure behavior of other Raman active bands. This may be related to a distortion of the (FeO_6) octahedral geometry induced by high pressure,

but further support for this explanation is required through single crystal EoS data and the Raman computational model.

The mode Grüneisen parameter is a very important thermodynamic parameter for describing the high-pressure–temperature behavior of minerals, providing a means by which the relative contributions of each vibration to the thermochemical properties of the mineral can be established (Anderson 2000). The parameter links the variation of frequency ν_i to the variation in crystal lattice volume $V(P, T)$, and also the effect of changing temperature on the size or dynamics of the lattice; thus, it is a function of pressure P for the isothermal state, or volume V for the isobaric state (Wagner 2000). As a result, the parameter not only provides the differing mass and ionic radius of substituting cations in magnesite, but also reflects the compressing effect of the carbonate ion.

For the isothermal state, the measured vibrational frequency ν_i as a function of pressure P represents a mode Grüneisen parameter for the phonon mode, as in the following equation (Born and Huang 1954):

$$\gamma_i = \frac{K_T}{\nu_{i,0}} \times \frac{\mathrm{d}\nu_i}{\mathrm{d}P},$$

where γ_i is the mode Grüneisen parameter, K_T is the isothermal bulk modulus, $\nu_{i,0}$ is each vibration frequency at ambient pressure, and $\mathrm{d}\nu_i/\mathrm{d}P$ is the slope of each vibration shift as a function of pressure.

The combined high-pressure Raman results ($\frac{\mathrm{d}\nu_i}{\mathrm{d}P}$) and the bulk modulus $K_0 = 97.5(11)$ GPa from the EoS studies of siderite are used to derive the mode Grüneisen parameter (γ_i), given in Table 2. The mode Grüneisen parameters for the two external lattice modes (T and L) are 1.61 and 1.39, respectively, and for the two internal modes (ν_1 and ν_4) are 0.22 and 0.27, respectively. Significantly, the Grüneisen parameters of the lower frequency lattice modes (T and L) of siderite are approximately five times greater than those of the higher frequency internal modes (ν_1 and ν_4), which is very close to the results in impurity-free magnesite (Liang et al. 2018a). However, the mode Grüneisen parameters (T, L, ν_4, and ν_1) obtained in this study are larger than those reported by Cerantola et al. (2015), although the relative relationship of each mode Grüneisen parameter is consistent. The difference in magnitude may arise from differences in the quality of Raman data acquisition and Lorentzian function fitting error; comparatively more data points were collected in this study to help ensure accurate and reliable results.

High-temperature Raman spectroscopy

High-temperature Raman spectra of the siderite single crystal were detected up to 300 °C (below its decomposition temperature), increasing in 20 °C increments at ambient pressure. Five Raman active bands, identified as translational lattice mode T, librational lattice mode L, in-plane bending internal mode ν_4, symmetric stretching internal mode ν_1 and out-of-plane bending mode $2\nu_2$, were observed within the temperature range of measurement. All five Raman bands decreased monotonically with increasing temperature without any splitting. The measured vibrational frequency $\nu_i(t)$ as the function of temperature t, given in Fig. 5 and data shown in Supplementary Table 5, is fitted as:

$$T(t) = 180.85\ [1 + (1.738 \times 10^{-6} - 7.804 \times 10^{-8} t)t],$$

$$V_{T,t} = 1.738 \times 10^{-6} - 7.804 \times 10^{-8} t,$$

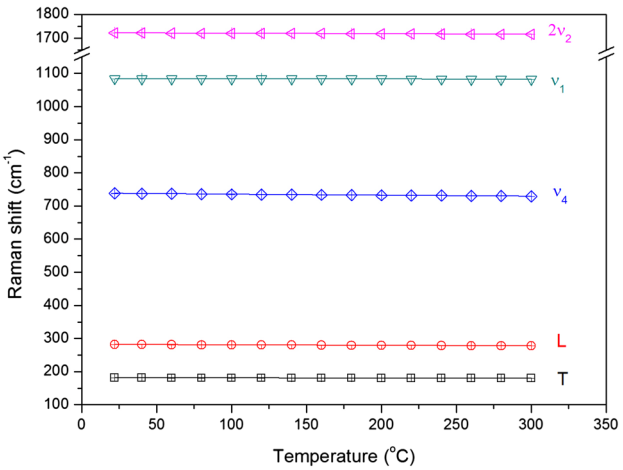

Fig. 5 High-temperature Raman spectra of siderite at ambient pressure

Table 2 $\frac{\mathrm{d}\nu_i}{\mathrm{d}P}$ and mode Grüneisen parameter γ_i of $FeCO_3$

Raman modes	$\nu_{i,0}$ (cm^{-1}) in this work	$\frac{\mathrm{d}\nu_i}{\mathrm{d}P}$ (cm^{-1}/GPa) in this work	Mode Grüneisen parameter (γ_i) in this work	$\frac{\mathrm{d}\nu_i}{\mathrm{d}P}$ (cm^{-1}/GPa) given by Cerantola et al. (2015)
T	180.872	2.99 (±0.02)	1.61 ± 0.01	2.51
L	281.842	4.01 (±0.02)	1.39 ± 0.01	3.82
ν_4	737.842	2.00 (±0.02)	0.27 ± 0.01	1.37
ν_1	1084.031	2.46 (±0.01)	0.22 ± 0.01	2.17
$2\nu_2$	1722.487	−0.824 (±0.005)	−0.0466 ± 0.0001	–

$$L(t) = 282.07\ [1 + (-4.478 \times 10^{-5} + 2.922 \times 10^{-8} t)t],$$
$$V_{L,t} = -4.478 \times 10^{-5} + 2.922 \times 10^{-8} t,$$

$$\nu_4(t) = 278.55\ [1 + (-4.632 \times 10^{-5} + 1.577 \times 10^{-8} t)t],$$
$$V\nu_{4,t} = -4.632 \times 10^{-5} + 1.577 \times 10^{-8} t,$$

$$\nu_1(t) = 1094.03\ [1 + (-1.734 \times 10^{-6} + 1.485 \times 10^{-10} t)t],$$
$$V\nu_{1,t} = -1.734 \times 10^{-6} + 1.485 \times 10^{-10} t,$$

$$2\nu_2(t) = 1722.46\ [1 + (-7.588 \times 10^{-6} + 1.335 \times 10^{-8} t)t],$$
$$V_2\nu_{2,t} = -7.588 \times 10^{-6} + 1.335 \times 10^{-8} t,$$

where $V\nu_{i,t} = 1/\nu_i\,(\mathrm{d}\nu_i/\mathrm{d}t)$ is the rate of each Raman frequency shift as a function of temperature. It can be seen from Fig. 5 that $V\nu_{4,t}$ and $V_{L,t}$, which are nearly linear, are about one order of magnitude larger than $V_{T,t}$, $V\nu_{1,t}$, and $V_2\nu_{2,t}$, and the rate of each Raman frequency shift with temperature $V\nu_{i,t}$ could be closely related to the linear thermal expansion ratio of Fe–O and C–O bond length.

Conclusion

A novel process has been devised to grow impurity-free siderite single crystals successfully, using high-temperature–pressure annealing. The structural data of impurity-free siderite single crystals could provide a standard rating scale in mineralogy for siderite research by avoiding the influence of impurities. Future research including single crystal growth of magnesite will be undertaken to prepare a series of solid solution $Mg_{1-x}Fe_xCO_3$ single crystals with various iron content. These will provide an ideal model for the systematic investigation of $Mg_{1-x}Fe_xCO_3$ structure, elasticity and conductivity.

Acknowledgements We acknowledge Jung-Fu Lin from University of Texas at Austin for constructive discussion in carbonate minerals. We thank Yong Meng and Jiali Cai from Institute of Geochemistry, Chinese Academy of Sciences, Guiyang for their valued assistance. This work was financially supported by Major State Research Development Program of China (2016YFC0601101), the Strategic Priority Research Program (B) of Chinese Academy of Sciences (XDB 18010401), and 135 Program of the Institute of Geochemistry (Y2ZZ041000), CAS.

References

Anderson OL (2000) The Grüneisen ratio for the last 30 years. Geophys J Int 143:279–294

Bischoff WD, Sharma SK, Mackenzie FT (1985) Carbonate ion disorder in synthetic and biogenic magnesian calcites—a Raman spectral study. Am Miner 70(5–6):581–589

Born M, Huang K (1954) Dynamical theory of crystal lattices. Oxford University Press, UK

Cerantola V, McCammon C, Kupenko I, Kantor I, Marini C, Wilke M, Ismailova L, Solopova N, Chumakov A, Pascarelli S, Dubrovinsky L (2015) High-pressure spectroscopic study of siderite ($FeCO_3$) with a focus on spin rossover. Am Miner 100:2670–2681

Cerantola V, Bykova E, Kupenko I, Merlini M, Ismailova L, McCammon C, Bykov M, Chumakov AI, Petitgirard S, Kantor I, Svitlyk V, Jacobs J, Hanfland M, Mezouar M, Prescher C, Ruffer R, Prakapenka VB, Dubrovinsky L (2017) Stability of iron-bearing carbonates in the deep Earth's interior. Nat Commun 8:15960

Dasgupta R, Hirschmann MM (2010) The deep carbon cycle and melting in Earth's interior. Earth Planet Sci Lett 298:1–13

Edwards HGM, Villar J, Jehlicka SE, J., and Munshi T (2005) FT-Raman spectroscopic study of calcium-rich and magnesium-rich carbonate minerals. Spectrochimica Acta Part A 61:2273–2280

Farfan G, Wang S, Ma H, Caracas R, Mao WL (2012) Bonding and structural changes in siderite at high pressure. Am Miner 97:1421–1426

French BM (1971) Stability relations of siderite ($FeCO_3$) in the system Fe–C–O. Am J Sci 27:37–78

Fu S, Yang J, Lin J-F (2017) Abnormal elasticity of single-crystal magnesiosiderite across the spin transition in Earth's lower mantle. Phys Rev Lett 118:036402

Gunasekaran S, Anbalagan G, Pandi S (2006) Raman and infrared spectra of carbonates of calcite structure. J Raman Spectrosc 37:892–899

Hazen RM, Finger L (1982) Comparative crystal chemistry: temperature, pressure, composition and the variation of crystal structure. Wiley, New York

Hazen RM, Prewitt CT (1977) Effects of temperature and pressure on interatomic distances in oxygen-based minerals. Am Miner 62:309–315

Hazen RM, Hemley RJ, Mangum AJ (2012) Carbon in Earth's interior: storage, cycling, and life. EOS Trans Am Geophys Union 93(2):17–18

Isshiki M, Irifune T, Hirose K, Ono S, Ohishi Y, Watanuki T, Nishibori E, Takata M, Sakata M (2004) Stability of magnesite and its high-pressure form in the lowermost mantle. Nature 427:60–63

Jana D, Walker D (1997) The impact of carbon on element distribution during core formation. Geochim Cosmochim Acta 61(13):2759–2763

Kaabar W, Botta S, Devonshire R (2011) Raman spectroscopic study of mixed carbonate materials. Spectrochim Acta Part A 78:136–141

Larson AC, Von Dreele RB (2004) General structure analysis system(GSAS). Los Alamos National Laboratory Report LAUR, pp 86–748

Lavina B, Dera P, Downs RT, Prakapenka V, Rivers M, Sutton S, Nicol M (2009) Siderite at lower mantle conditions and the effects of the pressure-induced spin-pairing transition. Geophys Res Lett 36:L23306

Lavina B, Dera P, Downs RT, Tschauner O, Yang W, Shebanova O, Shen G (2010a) Effect of dilution on the spin pairing transition in rhombo-hedral carbonates. High Press Res 30:224–229

Lavina B, Dera P, Downs RT, Yang W, Sinogeikin S, Meng Y, Shen G, Schiferl D (2010b) Structure of siderite $FeCO_3$ to 56 GPa and hysteresis of its spin-pairing transition. Phys Rev B 82:064110

Liang W, Liu QQ, Liu L, Kakeshita T, Uchida S, Jin CQ (2013) Growth of $Sr_2CuO_{3+\delta}$ superconductor single crystals at high pressure. Sci China Phys Mech Astron 56:691–693

Liang W, Li Z, Yin Y, Li R, Chen L, He Y, Dong H, Dai L, Li H (2018a) Single crystal growth, characterization and high-pressure Raman spectroscopy of impurity-free magnesite ($MgCO_3$). Phys Chem Miner **(in press)**

Liang W, Chen L, Wang L, Yin Y, Li Z, Li H (2018b) High pressure synthesis of siderite ($FeCO_3$) and its thermal expansion coefficient. High Temp High Press **(in press)**

Lin J-F, Tsuchiya T (2008) Spin transition of iron in the Earth's lower mantle. Phys Earth Planet Inter 170:248–259

Lin J-F, Liu J, Jacobs C, Prakapenka VB (2012) Vibrational and elastic properties of ferromagnesite across the electronic spin-pairing transition of iron. Am Miner 97:583–591

Litasov KD, Fei Y, Ohtani E, Kuribayashi T, Funakoshi K (2008) Thermal equation of state of magnesite to 32 GPa and 2073 K. Phys Earth Planet Inter 168:191–203

Liu QQ, Yang H, Qin XM, Yu Y, Yang LX, Li FY, Yu RC, Jin CQ, Uchida S (2006) Enhancement of the superconducting critical temperature of $Sr_2CuO_{3+\delta}$ up to 95 K by ordering dopant atoms. Phys Rev B 74:100506

Liu J, Lin J-F, Mao Z, Prakapenka VB (2014) Thermal equation of state and spin transition of magnesiosiderite at high pressure and temperature. Am Miner 99:84–93

Liu J, Lin J-F, Prakapenka VB (2015) High-pressure orthorhombic ferromagnesite as a potential deep-mantle carbon carrier. Sci Rep 5:7640

Lobanov SS, Goncharov AF, Litasov KD (2015) Optical properties of siderite ($FeCO_3$) across the spin transition: crossover to iron-rich carbonates in the lower mantle. Am Miner 100:1059–1064

Markgraf SA, Reeder RJ (1985) High-temperature structure refinements of calcite and magnesite. Am Miner 70:590–600

Mattila A, Pylkkänen T, Rueff JP, Huotari S, Vankó G, Hanfland M, Lehtinen M, Häääänen K (2007) Pressure induced magnetic transition in siderite $FeCO_3$ studied by X-ray emission spectroscopy. J Phys: Condens Matter 19:386206

McCammon C (2005) The paradox of mantle redox. Science 308:807–808

Merlini M, Sapelli F, Fumagalli P, Gatta GD, Lotti P, Tumiati S, Aabdellatief M, Lausi A, Plaisier J, Hanfland M, Crichton W, Chantel J, Guignard J, Meneghini C, Pavese A, Poli P (2016) High-temperature and high-pressure behavior of carbonates in the ternary diagram $CaCO_3$–$MgCO_3$–$FeCO_3$. Am Miner 101:1423–1430

Nagai T, Ishido T, Seto Y, Nishio-Hamane D, Sata N, Fujino K (2010) Pressure-induced spin transition in $FeCO_3$-siderite studied by X-ray diffraction measurements. J Phys Conf Ser 215:012002

Prescher C, Prakapenka VB (2015) DIOPTAS: a program for reduction of two-dimensional X-ray diffraction data and data exploration. High Press Res 35:285–288

Rividi N, van Zuilen M, Philippot P, Menez B, Godard G, Poidatz E (2010) Calibration of carbonate composition using micro-Raman analysis: application to planetary surface exploration. Astrobiology 10:293–309

Rohrbach A, Schmidt MW (2011) Redox freezing and melting in the Earth's deep mantle resulting from carbon-iron redox coupling. Nature 472:209–212

Rosenberg PE (1963) Synthetic solid solutions in the systems $MgCO_3$–$FeCO_3$ and $MnCO_3$–$FeCO_3$. Am Miner 48:1396–1400

Ross NL (1997) The equation of state and high-pressure behavior of magnesite. Am Miner 82:682–688

Rutt HN, Nicola JH (1974) Raman spectra of carbonates of calcite structure. J Phys C Solid State Phys 7:4522–4528

Schauble EA, Ghosh P, Eiler JM (2006) Preferential formation of C-13–O-18 bonds in carbonate minerals, estimated using first-principles lattice dynamics. Geochim Cosmochim Acta 70(10):2510–2529

Shannon RD, Prewitt CT (1969) Effective ionic radii in oxides and fluorides. Acta Crystallogr A B25:925–946

Shi H, Luo W, Johansson B, Ahuja R (2008) First-principles calculations of the electronic structure and pressure-induced magnetic transition in siderite $FeCO_3$. Phys Rev B 78:155119

Speziale S, Milner A, Lee VE, Clark SM, Pasternak MP, Jeanloz R (2005) Iron spin transition in Earth's mantle. Proc Natl Acad Sci 102(50):17918–17922

Spivak A, Solopova N, Cerantola V, Bykova E, Zakharchenko E, Dubrovinsky L, Litvin Y (2014) Raman study of $MgCO_3$–$FeCO_3$ carbonate solid solution at high pressures up to 55 GPa. Phys Chem Miner 41:633–638

Sturhahn W, Jackson JM, Lin J-F (2005) The spin state of iron in minerals of Earth's lower mantle. Geophys Res Lett 32(12):L12307

Wagner JM (2000) On the inadequacy of linear pressure dependence of vibrational frequency. Solid State Commun 116:355–356

Weis C, Sternemann C, Cerantola V, Sahle CJ, Spiekermann G, Harder M, Forov Y, Kononov A, Sakrowski R, Yavaş H, Tolan M, Wilke M (2017) Pressure driven spin transition in siderite and magnesiosiderite single crystals. Sci Rep 7:16526

Williams Q, Collerson B, Knittle E (1992) Vibrational spectra of magnesite ($MgCO_3$) and calcite-III at high pressures. Am Miner 77:1158–1165

Xia H, Yin Y, Dai J, Yang J, Qin X, Jin C, Long Y (2015) Magnetism and magnetocaloric effect study of $CaFe_{0.7}Co_{0.3}O_3$. Mater Res Express 2:046103

Yang J, Mao Z, Lin J-F, Prakapenka VB (2014) Single-crystal elasticity of the deep-mantle magnesite at high pressure and temperature. Earth Planet Sci Lett 392:292–299

Zhang J, Martinez I, Guyot F, Gillet P, Saxena SK (1997) X-ray diffraction study of magnesite at high pressure and high temperature. Phys Chem Miner 24:122–130

Zhang J, Martinez I, Guyot F, Reeder R (1998) Effects of Mg–Fe^{2+} substitution in calcite-structure carbonates: thermoelastic properties. Am Miner 83:280–287

Zhang L, Yan S, Jiang S, Yang K, Wang H, He S, Liang D, Zhang L, He Y, Lan X, Mao C, Wang J, Jiang H, Zheng Y, Dong Z, Zeng L, Li A (2015) Hard X-ray micro-focusing beamline at SSRF. Nucl Sci Technol 26:060101